Liquid Structure and Transport Properties of the Deep Eutectic Solvent Ethaline

Yong Zhang,[†] Derrick Poe,[†] Luke Heroux,[‡,¶] Henry Squire,[§] Brian W. Doherty,[‖] Zhuoran Long,[‖] Mark Dadmun,[⊥,#] Burcu Gurkan,[§] Mark E. Tuckerman,[‖,@,△] and Edward J. Maginn[*,†]

†*Department of Chemical and Biomolecular Engineering, University of Notre Dame, Notre Dame, IN 46556 USA*

‡*Department of Material Science and Engineering, University of Tennessee, Knoxville, TN 37996 USA*

¶*Oak Ridge National Laboratory, Neutron Sciences Division, Oak Ridge, TN 37831*

§*Department of Chemical and Biomolecular Engineering, Case Western Reserve University, Cleveland, Ohio 44106*

‖*Department of Chemistry, New York University, New York, NY 10012 USA*

⊥*Department of Chemistry, University of Tennessee, Knoxville, TN 37996 USA*

#*Oak Ridge National Laboratory, Chemical Sciences Division, Oak Ridge, TN 37831*

@*Courant Institute of Mathematical Science, New York University, New York, NY 10012 USA*

△*NYU-ECNU Center for Computational Chemistry at NYU Shanghai, 3663 Zhongshan Rd. North, Shanghai 200062, China*

E-mail: ed@nd.edu

Abstract

A range of techniques including physical property measurements, neutron scattering experiments, *ab initio* molecular dynamics and classical molecular dynamics simulations are used to probe the structural, thermodynamic, and transport properties of a deep eutectic solvent comprised of a 1:2 molar ratio of choline chloride and ethylene glycol. This mixture, known as ethaline, has many desirable properties for use in a range of applications and therefore understanding its liquid structure and transport properties is of interest. Simulation results are able to capture experimental densities, diffusivities, viscosities, and structure factors extremely well. The solvation environment is dynamic and dominated by different hydrogen bonding interactions. Dynamic heterogenities resulting from hydrogen bonding interactions are quantified. Rotational dynamics of molecular dipole moments of choline and ethylene glycol are computed and found to exhibit a fast and slow mode.

Introduction

Deep eutectic solvents (DESs) have emerged over the past decade as a potentially useful class of liquids for many applications including electrochemistry,[1] synthesis,[2] separations,[3] and catalysis.[4] DESs are often comprised of a mixture containing a quaternary ammonium halide salt that serves as a hydrogen bond acceptor (HBA) and a molecular compound that serves as a hydrogen bond donor (HBD). DESs share many similarities with ionic liquids (ILs), in that they have very low volatility and vast chemical diversity. Although making generalizations about DESs and ILs is difficult because of their chemical diversity, many DESs are less expensive and have lower toxicity when compared to conventional ILs.

One of the most commonly studied DESs is a 2:1 molar mixture of ethylene glycol (EG)/choline chloride (ChCl). This DES is commonly referred to as “ethaline” and is representative of a so-called “Type III” DES.[5] The physical properties of ethaline make it especially attractive for many applications. It has a relatively low viscosity, excellent solvation properties and a very low melting temperature. Several volumetric, thermal, and transport properties have been measured experimentally.[6–12] For some properties, the level of agreement between these different sets of measurements is relatively poor; it has been suggested that this is at least partly due to differences in water content between the different samples.[12]

In addition to having accurate physical properties of DESs, it is equally important to develop structure-property relationships that can help explain how certain chemical and structural features lead to particular performance properties. Several recent molecular simulation studies have been carried out to try to make this connection. These include *ab initio* molecular dynamics (AIMD) simulations[13,14] as well as force field-based classical molecular dynamics (CMD) simulations.[15–18]

While the experimental and computational studies mentioned here have greatly increased our molecular-level understanding of the interactions present in ethaline, most were focused on a small sub-set of properties or relied solely on a handful of experimental or computational methods. For example, Kaur et al.[18] performed extensive calculations to model the liquid structure of ethaline in the form of X-ray scattering structure factors, radial distribution functions, and spatial distribution functions, however the simulated results were not compared against experimental data. Other studies focused mainly on force field development and validation.[16,17] The water content of experimental ethaline results compared against is often unclear, and studies have indicated that dynamics of these parameterized models are highly sensitive to small amounts of water.[19] Orientational dynamics of DESs have not been widely examined, with only a few experimental studies addressing their importance[20–23] and no computational studies to date. Reuter *et. al* notes that these orientational dynamics can have a significant influence on translational dynamics and warrants further study of their link with structural characteristics. As a result, there are still many unanswered questions regarding the link between liquid structure and the properties of ethaline. For example, translational and rotational diffusivity measurements suggest that ethaline is dynamically heterogeneous but spatially homogeneous.[24]

Recently, Hammond, Bowron and Edler[25] studied the liquid structure of reline - a DES composed of 2:1 molar ratio of urea and ChCl. Their approach in combining neutron diffraction with empirical potential structure refinement to obtain radial distribution functions confirmed the previously hypothesised hydrogen bonding network in which Cl ions are solvated by two urea through the amine groups and one Ch molecule through the hydroxyl group. They postulate that the deep eutectic behavior originates from this observed dominant solvation structure around Cl where the charge is delocalized and strong interaction forces among species prevent crystallization.

Similarly, in this work, we seek to develop a more comprehensive picture of the structure and properties of ethaline using a wide array of experimental and computational methods including neutron scattering, physical property measurements, AIMD, and CMD simulations. Despite the increasing interest in ethaline DES in applications ranging from electrochemical synthesis and redox flow batteries[26–28] to gas separations, there has been no neutron studies examining its structure and detailing the nature of its hydrogen bonding network. Here, we demonstrate the simultaneous use of neutron scattering, physical property measurement, and molecular simulations as a powerful method to understand DES properties. We validate the CMD simulations against AIMD simulations and experimental property measurements and then use the CMD simulations to analyze coordination environments, spatial and structural heterogeneity, as well as local dynamics.

Experimental Methods

Density and Viscosity

Ethaline was prepared and physical properties characterized according to the previously outlined standard procedure.[29] Briefly, choline chloride (Acros Organics, 99%) was dried under vacuum for 12 hours at 125°C. Anhydrous ethylene glycol (Acros Organics, 99.8%)

was used as received and stored under a dry nitrogen atmosphere. Dried choline chloride and ethylene glycol were combined in a 1 to 2 molar ratio, respectively, inside of an argon filled glovebox (VTI, $H_2O < 0.1$ ppm and $O_2 < 0.1$ ppm) and mixed at 80°C for 2 hours. The homogeneous sample was slowly cooled and stored under a dry argon atmosphere to prevent water uptake. The water content of the sample was determined by coulometric Karl Fischer titration (Metrohm Coulometric KF 889 D) and found to be 75 ppm.

The temperature-dependent density was measured using an Anton Paar DMA 4500M vibrating tube density meter (accuracy of ± 0.00005 g/cm^{-3} and ± 0.03 K) with a sample size of 1 mL. Prior to the measurement, the tube was cleaned with methanol followed by deionized water, then dried with air. The density of air was checked at 298.15 K to confirm the tube was clean. Density data were collected in the temperature range of 298.15 K to 363.15 K.

Viscosity was measured using a Rheosense MicroVISC microchannel viscometer (accuracy of ±2%) coupled with a MicroVISC Temperature control unit (±0.1 K). Prior to the measurement, the microchannel was cleaned with methanol. Cannon oil standard (S20) was measured to confirm the reliability of measurements. Viscosities were measured in the temperature range of 298.15 K to 323.15 K in increments of 5 K. Average of triplicate viscosity measurements were reported.

Neutron Scattering

Deuterated chemicals for neutron scattering measurements, d-choline chloride (trimethyl-d9, 98%) and d-ethylene glycol(d6, 98%), were purchased from Cambridge Isotopes Laboratory, while protiated chemicals, ethylene glycol and choline chloride, were purchased from Sigma Aldrich. DES mixtures were prepared in a nitrogen filled glove box with $O_2 \leq 0.2$ ppm, where the ethylene glycol was heated to 333 K and then choline chloride was added in a 1:2 ratio, respectively. After a 1-hour solvation period, ethaline solutions were cooled to room temperature. These mixtures were sealed in 3mm diameter quartz capillaries with a height

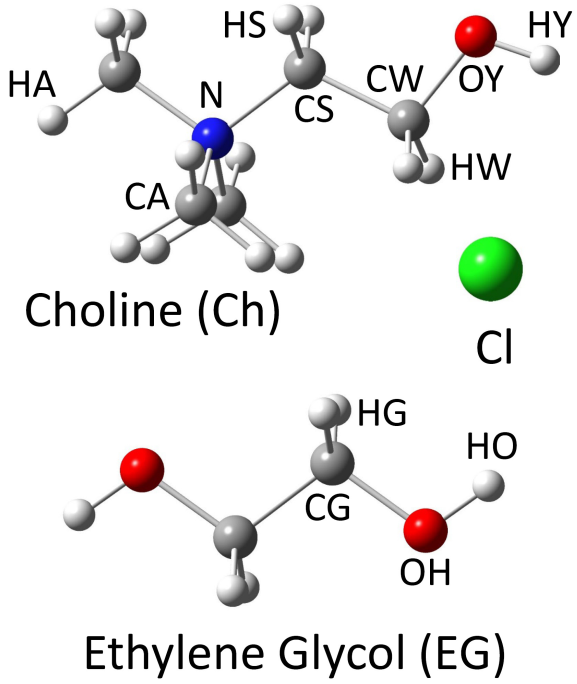

Figure 1: Structure and atom definitions of the three species comprising ethaline.

of at least 1.5 cm.

Neutron total scattering measurements were collected at the Nanoscale Ordered Materials Diffractometer (NOMAD) at Oak Ridge National Laboratory. The diffraction range covered from 0.1 $Å^{-1}$ up to 30 $Å^{-1}$. Measurements at 298 K were taken in 30-minute intervals and multiple sets of the same composition were summed together prior to reduction to improve statistics. $S(q)$ data were obtained by reduction of data using Addie. Quartz capillary background scattering was subtracted from sample scattering. All ethaline data were then normalized to scattering from vanadium.

Simulation Methods

Ab Initio Molecular Dynamics Simulations

The structure and atom definitions of ethaline used in the simulations are shown in Figure 1. Starting geometries for the AIMD simulations were prepared using CMD in the simulation package PINY_MD[30] with a previously developed force field for DES systems[17] in the canonical NVT ensemble for 50 ns. The ethaline system was constructed using the program Packmol[31,32] at a 1:2 molar ratio (8 choline chloride ions to 16 ethylene glycol molecules). The cubic box was kept constant with edge lengths of 14.9 Å that reproduced an extrapolated experimental density[33] at 400 K. AIMD simulations were carried out using density functional theory (DFT) within the CP2K package utilizing the QUICKSTEP module.[34] To calculate forces and energies on all atoms of each system, a hybrid Gaussian and planewave (GPW) approach was used with the molecular optimized triple- basis set (MOLOPT-TZVP-GTH),[35] along with the Perdew-Burke-Ernzerhof (PBE) functional and the corresponding Goedecker-Teter-Hutter (GTH) psuedopotentials.[36] A 420 Ry density cutoff with the finest grid level was set with a multigrid number 4 and REL_CUTOFF of 40 using the smoothing for the electron density (NN10_SMOOTH) and its derivative (NN10).[34] To include dispersion, an empirical dispersion correction was included (D3).[37] Trajectories were sampled using periodic boundary conditions and boxes were equilibrated for 15 ps with the canonical NVT ensemble at 400 K held using the Nosé-Hoover-chain thermostat.[38,39] Production runs were carried out for an additional 45 ps using a microcanonical NVE ensemble with a time step of 0.5 fs. Radial distribution functions (RDFs) and structure factor $S(q)$ were calculated using the TRAVIS program.[40]

Classical Molecular Dynamics Simulations

CMD simulations were carried out using the package LAMMPS.[41] The general Amber force field (GAFF)[42] was used to describe the interactions. The optimized molecular structures and atom types are shown in Figure 1. The partial charges derived by Perkins and coworkers[15] were adopted. The total charges of choline and chloride were scaled to ±0.9 e, respectively, to account for polarizability and charge transfer.[43] The long-range electrostatic interactions were calculated using the particle-particle particle-mesh (PPPM) method[44] with a real space cutoff of 12 Å. The same cutoff was used for van der Waals interactions and a tail correction[45] was applied.

The simulation box was built up by placing molecules randomly in a cubic box, again using the package Packmol.[31,32] The ethaline box contained 250 ChCl and 500 EG molecules, whereas the pure EG box contained 1000 EG molecules. To calculate the neutron scattering structure factor $S(q)$, a larger ethaline box was used which had 1000 ChCl and 2000 EG molecules. Each system was equilibrated for 2 ns in the isothermal-isobaric (NPT) ensemble followed by a 20 ns simulation in the canonical ensemble (NVT). The Nosé-Hoover thermostat with chain length of three was used to control the temperature[46] and an extended Lagrangian approach[47] was used to control the pressure. A time constant of 100 fs was used for both the thermostat and barostat. The pressure was fixed at one atmosphere in all constant pressure simulations with isotropic volume fluctuations. Periodic boundary conditions were applied in all directions and a time step of 1 fs was used in all simulations. Three independent trajectories were generated for each system to estimate the uncertainty in the calculated properties from the standard deviation. For viscosity, a bootstrap method was used to estimate the uncertainty.[48] An example LAMMPS input file is provided in the SI.

Results

Density of Ethylene Glycol and Ethaline

Experimentally measured densities as a function of temperature are shown in Figure 2 (top) for pure EG and Figure 2 (bottom) for ethaline. Experimental densities from previous studies[6,7,9,49–52] are also included for comparison. As shown in the plot, the density measurements from the current work agree very well with previous values.

The calculated densities from CMD simulations are also provided in Figure 2. For EG, the calculations slightly overestimate the density. The deviation is larger at low temperatures than at high temperatures. The largest deviation observed is 2.7% at 298 K. For ethaline, the calculated densities match the experimental results extremely well over the

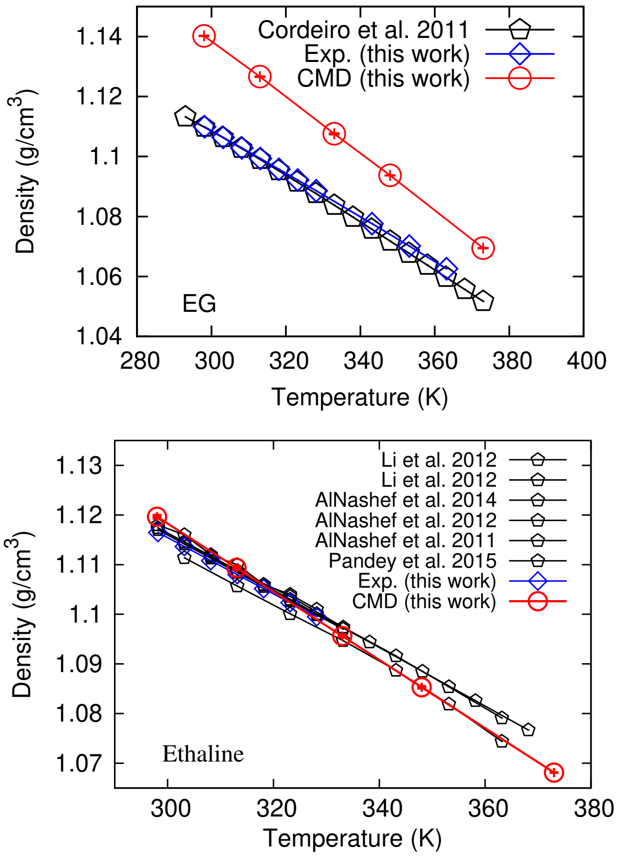

Figure 2: Comparison of experimental and simulated density as a function of temperature for ethylene glycol (top) and ethaline (bottom).

entire temperature range with a deviation smaller than 0.3%. This suggests that the applied classical force field is reasonable at capturing bulk property trends, although liquid density is not a very sensitive property to test force field accuracy. For this reason, additional steps were taken to validate the CMD simulations.

Validation of CMD against AIMD

With the density correctly captured, the accuracy of CMD simulations was further validated against AIMD. Based on both CMD and AIMD simulations, the neutron scattering structure

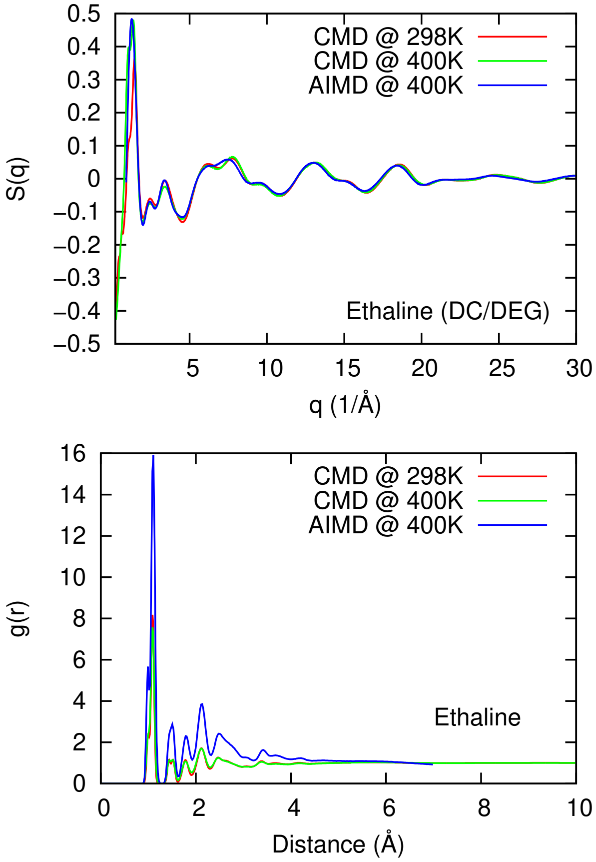

Figure 3: Comparison of simulated neutron scattering structure function of deuterated ethaline (top) and overall radial distribution function (bottom) from CMD and AIMD simulations.

function $S(q)$ was computed using

$$S(q) = \frac{\rho_0 \sum_i \sum_j x_i x_j f_i f_j \int_0^{L/2} 4\pi r^2 \left(g_{ij}(r) - 1\right) \frac{\sin qr}{qr} W(r) dr}{\left[\sum_i x_i f_i\right]^2} \tag{1}$$

where ρ_0 is the total number density, x_i and x_j are atomic mole fractions of atoms of types i and j, f_i and f_j are tabulated neutron scattering lengths,[53] L is the simulated box length, $g_{ij}(r)$ is the radial distribution function between atomic species of types i and j, and $W(r) = sin(2\pi r/L)/(2\pi r/L)$ is a Lorch function[54] used to reduce the effect of finite truncation of $g_{ij}(r)$ at large values of r. The CMD results at both 298 K and 400 K are compared to AIMD result at 400 K in Figure 3 (top) for deuterated choline (DC) and deuterated ethylene glycol (DEG). CMD results at 298 K and 400 K are almost identical except for some small deviations in the low q region and both agree with 400 K AIMD results, indicating that structural features in the system are captured by the force field and are insensitive to temperature over this range. The overall RDFs were also computed from both CMD and AIMD simulations and the comparison is shown in Figure 3 (bottom). Similar to $S(q)$, the CMD RDFs at 298 K and 400 K are nearly identical to each other. AIMD results show relatively high peak intensities, but the overall peak shapes and positions are similar to those of CMD results. Representative partial RDFs and the corresponding coordination numbers (CNs) were also calculated using both CMD and AIMD. The results shown in the Supporting Information (SI) (Figures S1 and S2) exhibit good agreement with minor deviations in peak height and CNs. For interactions involving chloride with choline or ethylene glycol, a distance shift is observed from 2.3 Å for CMD to 2.1 Å for AIMD. This shift in peak distance has been observed in a previous AIMD study of glyceline by Korotkevich *et al.*,[55] and can be attributed to the inclusion of polarization effects in the AIMD methodolgy. Considering the computational expense, we were not able to perform AIMD simulations at ambient temperatures and obtain well equilibrated results. The $S(q)$ and RDF comparison at 400 K, however, suggests that the CMD simulations will yield liquid structures and coordination numbers that are very similar to those that would be obtained with AIMD simulations. The remainder of the paper will therefore focus on comparing results from CMD simulations with experiment and using the CMD simulations to obtain information on local structure and dynamics as well as dynamical heterogeneity.

Liquid Structure

The computed $S(q)$ for different ethaline contrasts based on CMD simulations at 298 K are provided in Figure 4 and compared with experimental neutron scattering results.

The noise of the neutron data and variation in sample size contribute to subtle differences between the calculated and experimental scattering curves. However, the agreement between the neutron and simulation studies is quite strong, where the peaks associated with specific

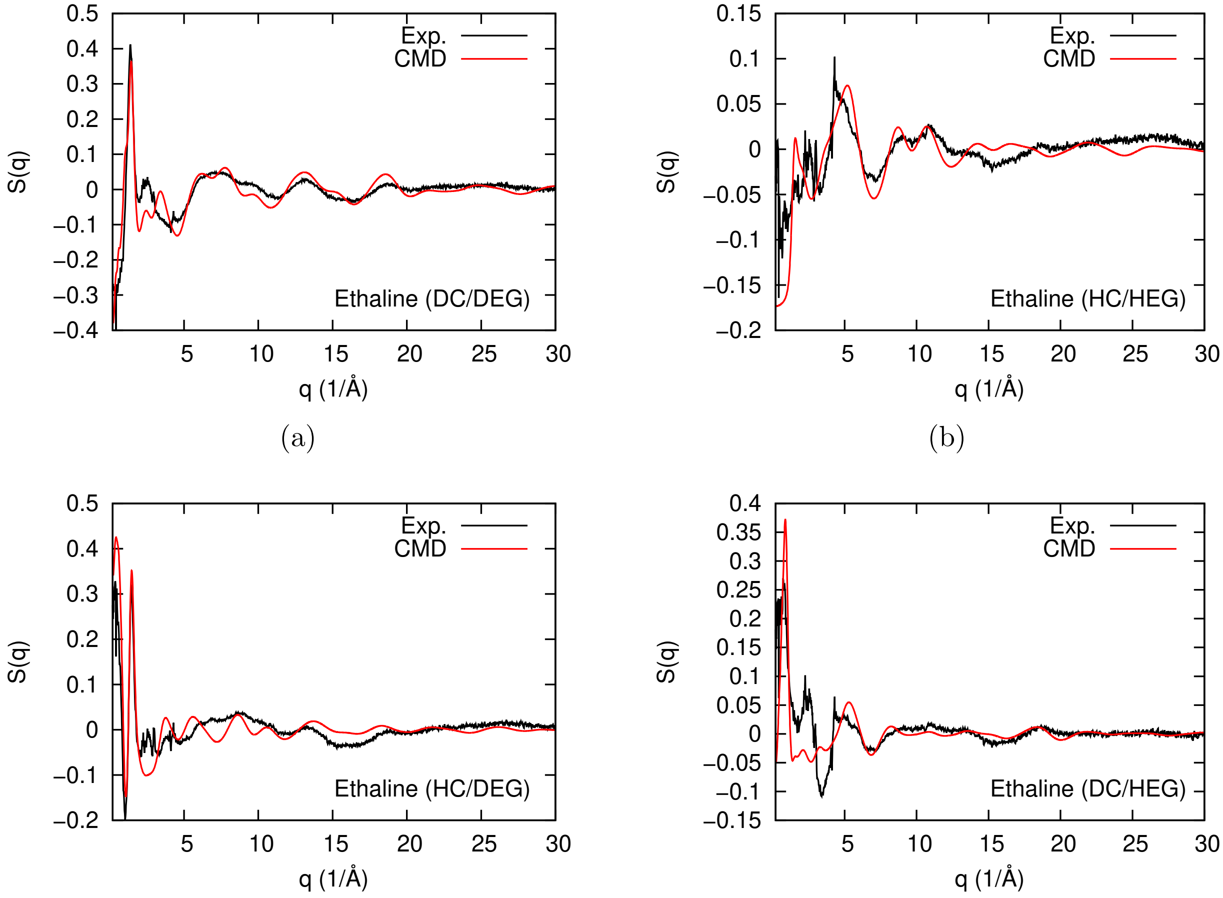

(a) (b)

(c) (d)

Figure 4: Comparison of experimental and computed structure factors for ethaline at 298 K. Deuterated EG and ChCl (a), protiated EG and ChCl (b), deuterated EG and protiated ChCl (c), protiated EG and deuterated ChCl (d).

structural correlations within and between components show up in both data sets at all length scales. Some discrepancies do exist between the experimental $S(q)$ curves and the simulations (Figure 4). Most notably between 2 Å^{-1} and 4 Å^{-1}, there is a single peak in the experimental diffraction data that appears as a double peak in the simulations. The intense broad peak at 2.5 Å^{-1} appears in samples with deuterated choline chloride (Figure 4), whereas the sharper peak at 3.5 Å^{-1} does not appear in the deuterated choline chloride experimental data. In contrast, the 2.5 Å^{-1} peak is suppressed in the protiated choline chloride samples and the 3.5 Å^{-1} peak appears (Figure 4b). We believe these variations between the experiment and simulation are related to the fact that d-choline chloride (DC) is only partially deuterated, as these discrepancies dominate in the samples with deuterated choline chloride. It appears that the consequence of this partial deuteration on the experimentally determined structure factor is not fully captured by the simulations. This interpretation is further supported when comparing the scattering of protiated choline chloride (HC) in deuterated ethylene glycol (DEG) and deuterated choline chloride in protiated ethylene glycol (HEG). In the results of protiated choline chloride and deuterated ethylene glycol (Figure 4c), both experimental and simulation results exhibit double peaks, albeit, with varying intensity. In the sample with deuterated choline chloride and ethylene glycol (Figure 4d), the 3.5 Å^{-1} peak is again non-existent in the experimental data, but the neutron data agrees with the 2.5 Å^{-1} peak from both simulations. While the source of these discrepancies is interesting, the global agreement of the neutron and simulation data sets provides strong evidence that the simulation data provides a robust representation of the molecular and nanoscale structure of ethaline.

The detailed liquid structure was further studied using CMD simulations. Figure 5 focuses on the interactions that involve Cl. Figure 5(a) shows the partial RDFs between Cl and hydroxyl hydrogens in both Ch (HY) and EG (HO) as well as the aliphatic hydrogen in EG (HG). See Figure 1 for atom type definitions. Both Cl-HY and Cl-HO RDFs show a sharp peak at 2.2 Å, suggesting strong interactions. As expected, the Cl-HG RDF has a much lower peak at a longer distance due to weaker interactions. Figure 5(b) shows the integrals of the RDFs, which give coordination numbers (CNs) as a function of radial distance. The CNs in the first solvation shell of Cl, defined by the first minimum between the first two maxima, are 0.70 for HY and 2.5 for HO. These CNs are consistent with the number of hydroxyl groups in Ch and EG, considering the 1:2 ratio between Ch and EG and that there are two hydroxyl groups in each EG, whereas only one in Ch. While Figure 5(b) only shows the average CNs, Figure 5(c) shows the probability of different CNs surrounding a Cl ion. As shown in the plot, a Cl ion is not coordinated by any HY atoms about 45% of the time and there is one HY atom in its first solvation shell roughly 40% of the time. There is also a small probability ($\sim$10%) to find two HY atoms in the first solvation shell of Cl. The picture

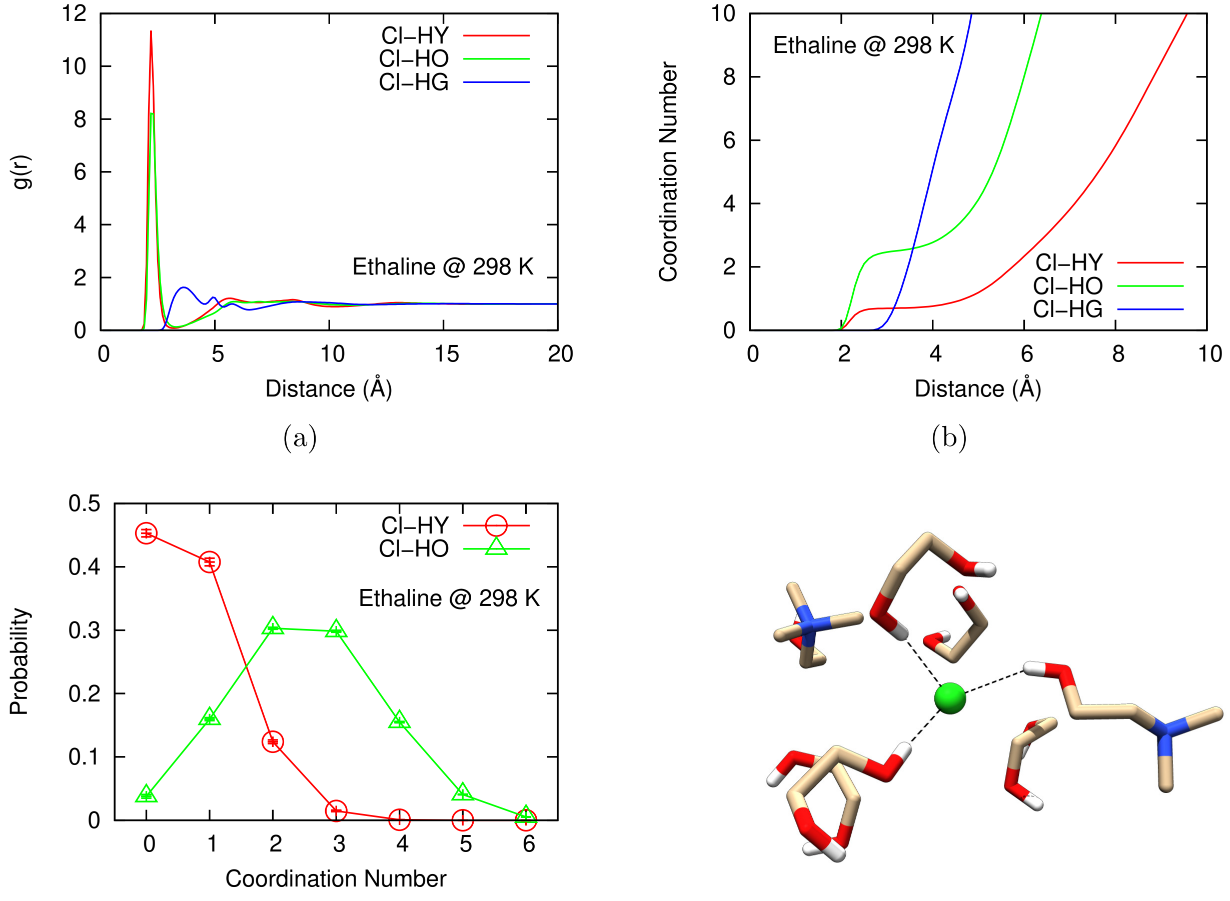

(a)

(b)

(c)

(d)

Figure 5: Computed radial distribution functions for a central Cl^- ion with respect to three different H-groups (a), coordination number as a function of distance about a central Cl^- ion (b), the probability of different numbers of coordinating H-groups about a central Cl^- ion (c), and a representative snapshot from a CMD simulation of the local environment about a Cl^- ion (color code: green - Cl^-; red - O; blue - N; yellow - C; white - H) (d).

is different for Cl-HO interactions, where the preferred configuration is a Cl coordinated by 2 or 3 HO atoms. In addition, there are significant numbers of Cl that are coordinated by 1 or 4 HO atoms, whereas only 4% of Cl does not have any HO in its first solvation shell. For the EG molecules in the first solvation shell of a Cl, 83% of them interact with Cl through one of the two hydroxyl groups (mono-dentate) and only 17% form bi-dentate interactions (see Figure S3 in SI). A representative snapshot of the Cl solvation environment is provided in Figure 5(d). This picture is very different from that reported previously for reline that each Cl is coordinated by two urea molecules while Ch is fully dissociated from Cl.[25]

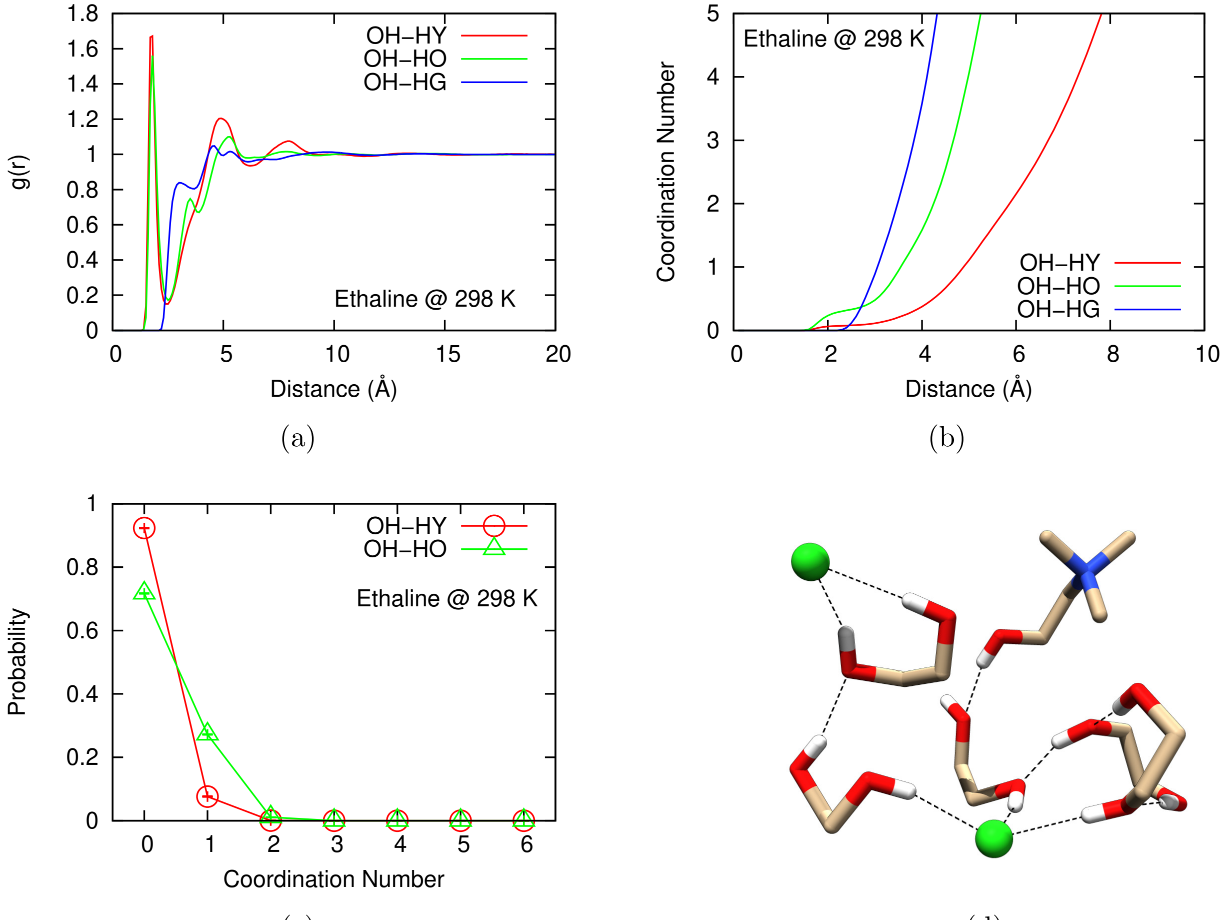

(a)

(b)

(c)

(d)

Figure 6: Computed radial distribution functions for a central OH-group of EG with respect to three different H-groups (a), coordination number as a function of distance about a central OH-group of EG (b), the probability of different numbers of coordinating H-groups about a central OH-group of EG (c), and a representative snapshot from a CMD simulation of the local environment about an OH-group of EG (color code: green - Cl^{-}; red - O; blue - N; yellow - C; white - H) (d).

The solvation environment of OH atoms in EG was also studied and the results are summarized in Figure 6. Similar to the case of Cl, both OH-HY and OH-HO RDFs show a sharp peak at very short distance (see Figure 6(a)). The peak is at 1.8 Å, however, a shorter distance due to the smaller size of O than Cl, and a much lower intensity. The OH-HG interaction does not have much specific structure. As shown in Figure 6(b), the CN of HY atoms in the first solvation shell of an OH atom was found to be 0.1 and that of HO is 0.3; both are much lower than those in the Cl solvation shell, suggesting relatively weaker interactions between OH and the hydroxyl hydrogen atoms compared to those between Cl and hydroxyl hydrogens. Further analysis reveals that over 90% of OH atoms do not have direct interactions with HY and the other 10% have one in the first solvation shell (see Figure 6(c)). Similarly, about 70% of OH atoms do not have direct interactions with HO atoms and roughly 30% have one interaction. There is a very small amount of OH atoms that have more than two HY or HO atoms in the first solvation shell. Almost all of the interactions with OH were found to be mono-dentate (see Figure S3 in SI). The snapshot shown in Figure 6(d) shows a representative hydrogen bond (HB) network in ethaline.

Similar analysis was also carried out for the interactions between OY and hydroxyl or aliphatic hydrogens, which were found to be weak and no highly preferred structure was identified. The results are shown in Figure S4 in the SI.

It is widely accepted that HBs play important roles in determining the thermodynamic properties in DES.[5] The above discussion reveals that, in ethaline, Cl is the strongest HB acceptor followed by OH atoms in EG. OY atoms in Ch are the weakest. To have a better understanding of ethaline, the HBs between EG molecules in ethaline and pure EG are compared. Figure 7(a) shows the partial RDFs between OH-HO and OH-HG. It is interesting to notice that the overall shapes in terms of peak and well positions of both RDFs are very similar in ethaline and pure EG. The peak heights are slightly depressed in ethaline, suggesting less organized structure. As shown in Figure 7(b), the difference is more significant in the calculated CNs due to the relatively low number density of EG in ethaline. In pure EG, each OH atom is hydrogen bonded by one HO atom. This number decreases to only 0.3 in ethaline, suggesting about 70% of the HBs are broken upon the addition of ChCl, although ChCl only accounts for one-third of the molecules in ethaline. In either ethaline or pure EG, OH-HG does not have a well defined configuration. Not surprisingly, the CN distribution in ethaline and pure EG also show significant differences. In pure EG, the majority of OH atoms (about 70%) form one HB with HO atoms while about 10% form two such HBs. Most OH is also surrounded by 2-4 HG atoms. Less than 10% of OH do not see HG atoms in the

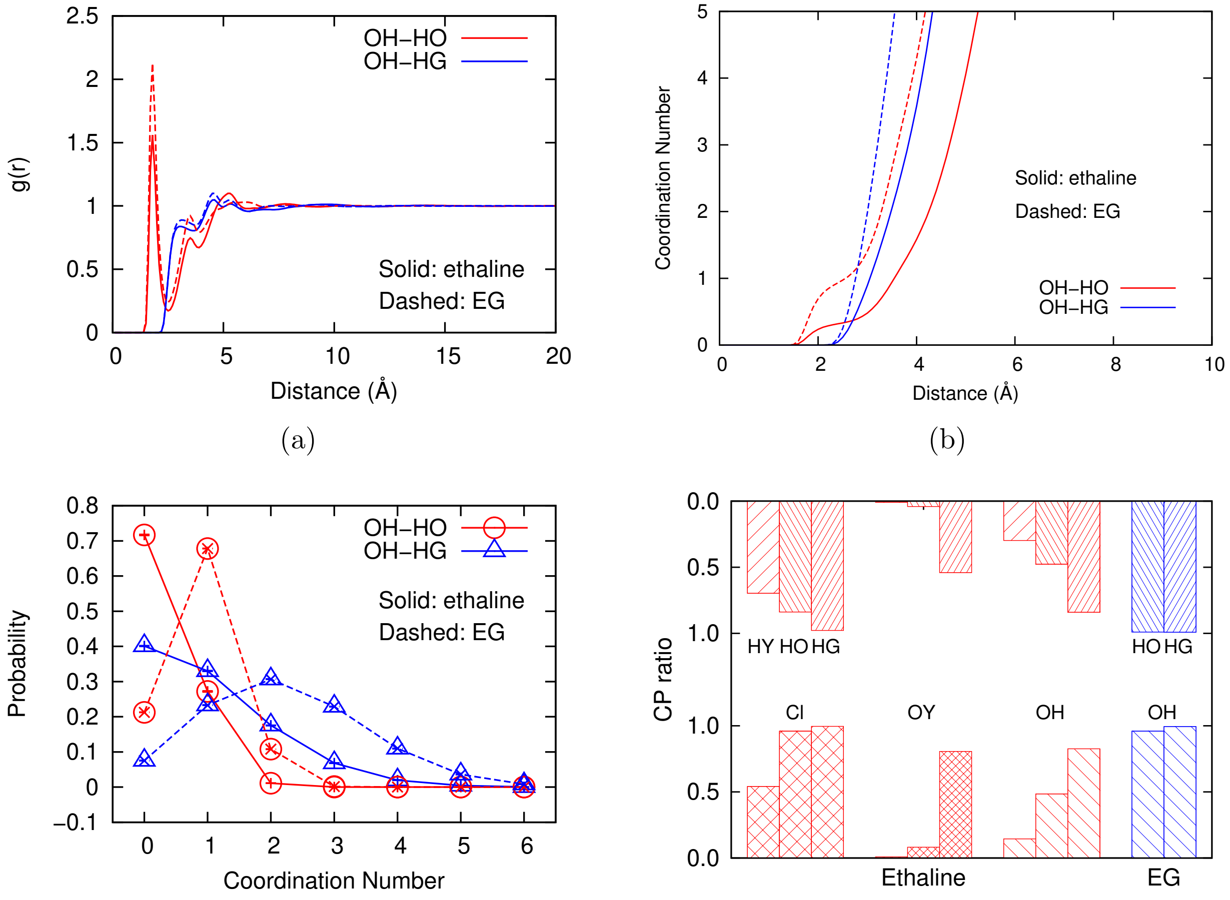

(a) (b)

(c) (d)

Figure 7: Comparison of the site-site radial distribution function for a central OH-group of EG with respect to the same OH-group and the alkyl hydrogen of EG in pure EG and ethaline (a), coordination number as a function of distance about a central OH-group of EG in pure EG and ethaline (b), the probability of different numbers of coordinating H-groups about a central OH-group of EG in pure EG and ethaline (c), and the number of contact pairs of each different species in pure EG (blue) and ethaline (red) (d).

first solvation shell. In ethaline, on the other hand, over 70% of OH do not have any HO in their first solvation shell and almost no OH form two HBs with HO atoms. The distribution of HG CNs is also shifted to lower values.

With three hydrogen bond acceptors and three hydrogen bond donors in the liquid, the HB interaction can be very complicated in ethaline. Figure 7(d) quantitatively summarizes these interactions. Each column in the plot corresponds to one interaction pair with the bottom bar presenting the ratio of the acceptor atoms involved in the interaction and the top bar presenting the donor hydrogen ratio. The results in pure EG are also included for comparison. Note that the ratios for the acceptor and donor in one interaction pair do not have to be the same. In pure EG, as shown in the plot, almost all the OH atoms form close contact pairs with both HO and HG atoms. Meanwhile, all the HO and HG atoms also form direct contact pairs with OH atoms. Therefore in pure EG, all the molecules are connected through HBs. Upon addition of ChCl, this HB network is broken significantly. As shown in the plot, about half of OH atoms still have close interaction with HO atoms and the other half have lost their contacts. Similarly, half of HO atoms have also lost their contacts with OH atoms. Due to the weaker interaction and longer cutoff distance, the reduced interaction of OH-HG pairs is less significant. On the other hand, Cl in ethaline replaces the role of OH in pure EG and almost all Cl, HO and HG atoms interact with each other. It is also observed from the plot that the ratios of atoms involved in Cl interactions are higher than those involving OY or OH atoms, suggesting Cl is a stronger HB acceptor. For the same reason, OY is the weakest HB acceptor, consistent with earlier discussion.

Figure 8 shows the computed spatial distribution functions (SDFs) for both ethaline and pure EG, in which the complex interactions between the molecules are presented in three dimensions. It is obvious that the EG molecules solvating the -OH groups in EG are largely replaced by Cl and Ch in ethaline. Cl takes the inner layer whereas Ch locates on the outer layer, consistent with earlier discussions.

Transport Properties

The transport and dynamic properties of ethaline were studied experimentally and with CMD simulations. The experimentally measured shear viscosity of pure EG and ethaline as a function of temperature are shown in Figure 9. Available measurements from previous studies are also included. For pure EG, the results from the current study agree with previous values[56] very well. For ethaline, the current results show systematically higher viscosities than previous values[57] by 5-8 cP. We believe this is due to the fact that our samples were

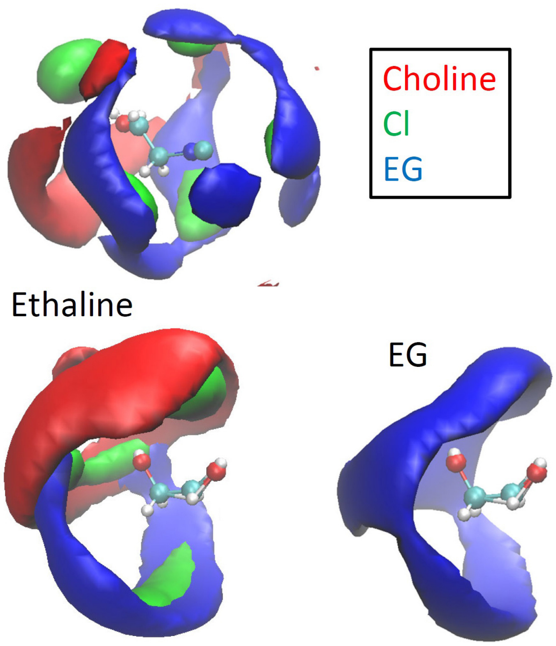

Figure 8: Three dimensional spatial distribution function of the different species in ethaline about a central choline ion (top) and spatial distribution functions about a central EG molecule in ethaline (bottom left) and in pure EG (bottom right). For clarity, the distribution about only one OH- group of EG is shown.

extremely dry, whereas samples from some previous studies were known to contain significant amounts of water. For both pure EG and ethaline, the viscosity decreases with increasing temperature. By adding ChCl into EG, the viscosity increases dramatically.

Using the time decomposition method,[58] the viscosity was computed for both pure EG and ethaline using CMD simulations from the integral over time of the pressure tensor autocorrelation function

$$\eta = \frac{V}{6k_BT} \sum_{\alpha \leq \beta} \int_0^\infty \langle \bar{P}_{\alpha\beta}(t) \cdot \bar{P}_{\alpha\beta}(0) \rangle \, \mathrm{d}t \tag{2}$$

where V is the system volume, k_B is the Boltzmann constant, T is temperature, and $\bar{P}_{\alpha\beta}$ denotes an element $\alpha\beta$ of a modified pressure tensor. In particular, in order to improve the statistics in the calculated viscosity, the pressure tensor elements $\bar{P}_{\alpha\beta}$ in Eq. 2 are chosen as follows: $\bar{P}_{xy} = P_{xy}$, $\bar{P}_{yz} = P_{yz}$, $\bar{P}_{xz} = P_{zx}$, $\bar{P}_{xx} = 0.5(P_{xx} - P_{yy})$, $\bar{P}_{yy} = 0.5(P_{yy} - P_{zz})$, and

$\bar{P}_{zz} = 0.5(P_{xx} - P_{zz})$, where $P_{\alpha\beta}$ are the elements of the standard pressure tensor. As Eq. 2 indicates, the results are then averaged over these six independent pressure-tensor element correlation functions.[59] The calculated shear viscosities are shown in Figure 9. The simulations underestimate the viscosity of pure EG and overestimate the viscosity of ethaline, but the trend in the computed results with temperature agrees with the experiments. Simulations also captured the trend that the viscosity increases significantly when ChCl is added to pure EG. This is consistent with the observations that Cl forms stronger interactions with EG than those between EG molecules.

Figure 10 shows the measured self-diffusion coefficients for Ch and EG in ethaline as a function of temperature. The self-diffusion coefficients were also derived from mean squared displacement (MSD) of the center of mass of each species based on CMD simulations using the Einstein relation

$$D_s = \frac{1}{6}\lim_{t\to\infty}\frac{d}{dt}\frac{1}{N}\sum_{i=1}^{N}\left\langle|\mathbf{r}_i(t) - \mathbf{r}_i(0)|^2\right\rangle \tag{3}$$

where $\mathbf{r}_i(t)$ is the center of mass position of species i at time t, and N is the number of individual species. The results are included in Figure 10 and compared to experimental values. For the studied temperature range, the calculated results agree with experiments very well. For both experimental and calculated results, the self-diffusion coefficients increase with increasing temperature, consistent with viscosity trend that the dynamics in the liquid becomes faster at higher temperatures. It is also observed from both experiments and simulations that the diffusion of EG is faster than that of Ch. The self-diffusion coefficient of Cl was calculated from simulation and was found to be between Ch and EG (see Figure S5 in the SI), consistent with previous simulation studies.[19] Computational studies of the dynamics of ethaline at multiple temperatures consist of a handful of sources. Results from this study match well with viscosities[17,19] and diffusivities[15–17,19] reported in previous studies of ethaline, with the added capability of accurately modelling pure EG dynamics with the same model.

While MSD and self-diffusion coefficients measure the average dynamics of the molecules,

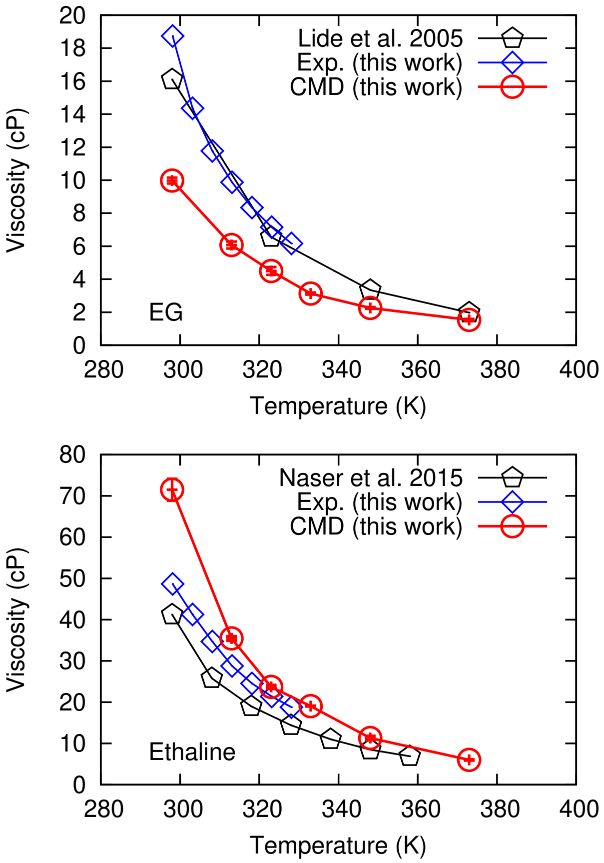

Figure 9: Comparison of experimental and simulated viscosity as a function of temperature for ethylene glycol (top) and ethaline (bottom).

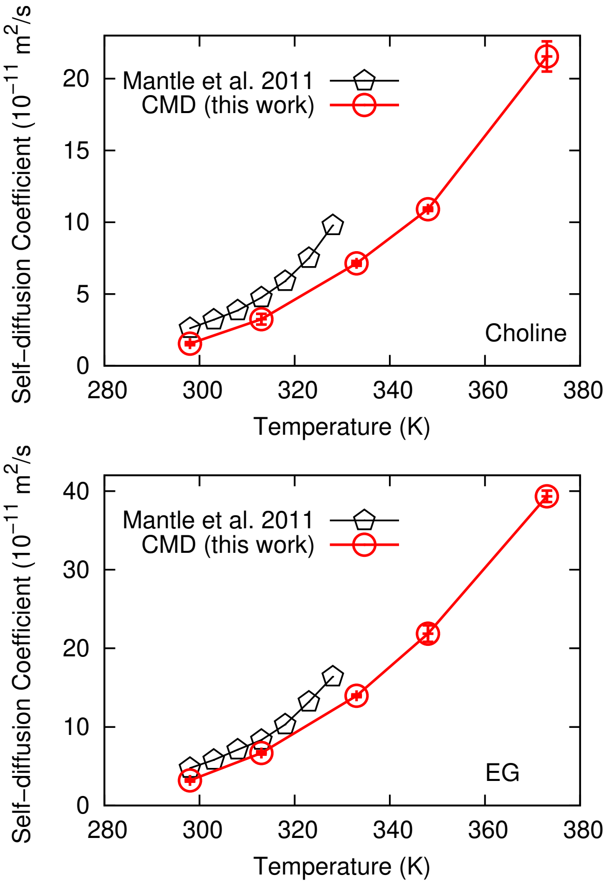

Figure 10: Comparison of experimental and simulated self-diffusivity as a function of temperature for choline (top) and EG (bottom) in ethaline.

it is of interest to study the distribution of dynamics, too. This is done by calculating the self-part of the van Hove function[60,61]

$$G_s(r,t) = \frac{1}{N}\sum_{i=1}^{N}\langle \delta(r - |\mathbf{r}_i(t) - \mathbf{r}_i(0)|)\rangle \tag{4}$$

where $4\pi r^2 G_s(r,t)$ is the probability that a particle has moved a distance r within the time t. Based on CMD simulations, the van Hove function was computed for the center of mass of each component in ethaline as well as pure EG and the results are provided in Figure S6 in SI. For a dynamically homogeneous system, the self part of the van Hove function follows a Gaussian distribution. Therefore, the deviation from Gaussian behavior is a measure of the dynamic heterogeneity. This heterogeneity can be quantified by the non-Gaussian parameter

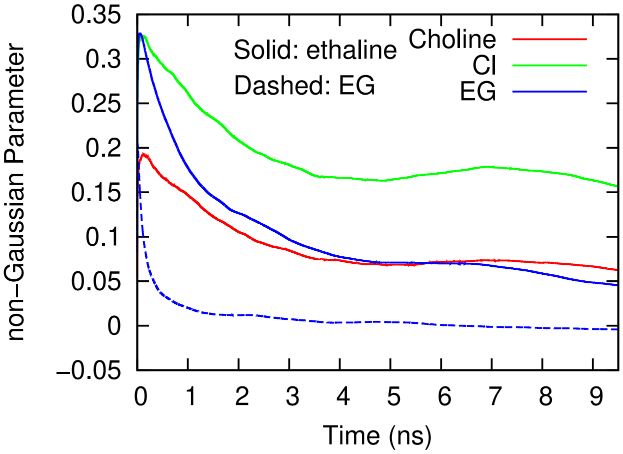

Figure 11: Non-Gaussian parameter for different species as a function of time in ethaline (solid) and EG (dashed) calculated at 298 K.

defined as

$$\alpha(t) = \frac{3\langle r^4(t)\rangle}{5\langle r^2(t)\rangle^2} - 1. \tag{5}$$

The timescale over which a system exhibits dynamic heterogeneity corresponds to the time during which $\alpha(t)$ is non-zero. Figure 11 shows the non-Gaussian parameter computed for each species in ethaline and pure EG at 298 K. As shown in the figure, $\alpha(t)$ in pure EG decays to zero in less than 2 ns. In ethaline, on the other hand, after 9.5 ns, $\alpha(t)$ did not fully decay to zero. The decay for Cl is even slower than for that of Ch and EG, suggesting that the dynamics of Cl is more heterogeneous than Ch and EG. This is likely related to the more complicated solvation structure of Cl, as shown in Figure 5(c).

As discussed earlier, there are different types of HB interactions in ethaline with various strengths. It is likely that these HBs show different dynamic properties as well. Using the package Travis,[40] the HB dynamics in ethaline and pure EG was studied based on CMD simulations following the time autocorrelation function

$$C_{HB}(t) = \left\langle \frac{h_{ij}(0)h_{ij}(t)}{h_{ij}(0)^2} \right\rangle \tag{6}$$

where $h(t)$ is unity when a particular HB is formed at time t and zero otherwise. The derived time constants are summarized in Table 1. The cutoff distance that defines each HB interaction as well as the CN of donor hydrogens are also included in the table. The HB dynamic time constants do show clear heterogeneity. The HBs involving Cl and the Ch and EG hydroxyl hydrogens have significantly longer time scales than others and are quite different, suggesting stronger interactions. This is consistent with the earlier discussion. Comparing the HBs in pure EG to the same ones in ethaline, the life times of the HBs are about three times longer in the latter, which is consistent with the lower viscosity and faster diffusivity of pure EG relative to ethaline observed in both experiments and simulations.

Table 1: Hydrogen bond dynamics time constant (ps) computed based on CMD simulations at 298 K

	r_{cutoff} (Å)	CN	time constant (ps)
	ethaline		
Cl-HY	3.2	0.70	1462.4 ± 56.0
Cl-HO	3.3	2.52	972.4 ± 27.9
Cl-HG	4.6	8.32	113.6 ± 0.5
OH-HY	2.5	0.08	25.4 ± 1.5
OH-HO	2.3	0.30	80.5 ± 0.5
OH-HG	3.1	1.10	28.1 ± 0.8
OY-HY	2.4	0.01	24.1 ± 0.8
OY-HO	2.5	0.09	25.1 ± 1.6
OY-HG	3.5	2.08	53.8 ± 1.7
	pure EG		
OH-HO	2.4	0.93	32.1 ± 0.3
OH-HG	3.1	2.46	10.4 ± 0.0

Finally, the rotational dynamics of the molecular dipole moment in ethaline and pure EG were studied using the correlation function

$$C(t) = \left\langle \frac{1}{2N_{\mathrm{i}}} \sum_{i=1}^{N_{\mathrm{i}}} \left[3\cos^2\theta_i(t) - 1\right] \right\rangle \tag{7}$$

where θ_i is the angle between the ith molecular dipole moment at time t and time zero, and N_{i} is the number of species i in the system. Based on CMD simulations, the correlation functions calculated for Ch and EG in ethaline at 298 K are shown in Figure 12. The correlation function for Ch decays much slower than that of EG, consistent with the trend that Ch diffuses slower than EG as shown in Figure 10. The correlation function for pure EG is also included for comparison. Obviously, the decay of the EG correlation function is much faster in pure EG than that in ethaline, consistent with both experimental and simulation observations that ethaline has a higher viscosity and slower dynamics than pure EG. The correlation functions in Fig. 12 exhibit clear fast and slow decays that are not necessarily exponential. We, therefore, chose to fit them to the following functional form:

$$C(t) = b_1 E_{\alpha_1}(-(t/\tau_1)^{\alpha_1}) + b_2 E_{\alpha_2}(-(t/\tau_2)^{\alpha_2}) \tag{8}$$

where $E_\alpha(z)$ is a Mittag-Leffler function,

$$E_\alpha(z) = \sum_{n=0}^{\infty} \frac{z^n}{\Gamma(\alpha + 1)}, \tag{9}$$

which can also be expressed as a Laplace transform of the form[62,63]

$$E_\alpha(-z^\alpha) = \frac{1}{\pi} \int_0^\infty e^{-xz} \frac{x^{\alpha-1} \sin(\pi\alpha)}{x^{2\alpha} + 2x^\alpha \cos(\pi\alpha) + 1} \, \mathrm{d}x, 0 < \alpha < 1, \tag{10}$$

and b_n ($b_1 + b_2 = 1$), α_n, and τ_n, $n = 1, 2$, are the fitting parameters, with τ_n capturing relevant time scales in the system. In eq. (9), $\Gamma(x)$ is the Gamma function. The fits are provided in Figure S7 in the SI and the fitted parameters are summarized in Table 2. The high quality of the fits, as indicated by the R^2 values in Table 2 indicate that the correlation functions do, indeed, exhibit decay on two well-separated time scales.

Note that Mittag-Leffler functions generally emerge as the solutions to fractional kinetic models and fractional rate equations.[64–67] As eq. (9) indicates, $E_\alpha(z)$ is an exponential when $\alpha = 1$, but more generally, $E_\alpha(z)$ behaves as a stretched exponential for small z, $E_\alpha(-(t/\tau)^\alpha) \approx \exp(-(t/\tau)^\alpha)/\Gamma(1+\alpha)$, and then decays asymptotically according to a power law $(t/\tau)^{-\alpha}$. As Table 2 suggests, the slow process for Ch and pure EG is very close to exponential while that for EG in ethaline deviates from exponential behavior a bit more significantly. We might expect this based on the fact that $\alpha = 1$ corresponds to two-dimensional diffusion, and rotational diffusion of a single vector occurs along two angular directions. The fast processes, however, are clearly non-exponential, and the value of α, which lies between 1/2 and 1, places these fast processes somewhere between one- and two-dimensional rotational diffusion. The quality of the fits to this fractional kinetic model suggests some intriguing underlying physics, which has been observed in other electrolyte system,[68] that merits further investigation and will be the subject of future work.

Having extracted the relevant time scales for orientational dynamics, it is worth discussing what the time scales τ_1 and τ_2 represent. For Ch, the short time process τ_2 is on the order of 20 ps, similar to HB lifetimes between OH-HY and OY-HY groups. As the Ch ion rotates, it makes and breaks HBs on about this time scale. The longer time process, τ_1 is over 300 ps, and we believe it is associated with the overall rotational decorrelation of the Ch dipole moment. This time scale is closely related to the long-axis rotational motion of the Ch ion. The long-time HB lifetime for Cl with Ch may also contribute to this time scale. For the smaller EG molecule, the time scales are much faster than for Ch. Note that the EG molecule is almost symmetric and bears a very small dipole moment. Therefore its dipole moment rotational dynamics is sensitive to both intermolecular interactions and internal configuration changes. The short time process for EG in ethaline, τ_2, is on the order of 1 ps, which we assign to local intramolecular relaxation of the EG molecule. In pure EG, τ_2 is about twice as fast, consistent with the lower viscosity of pure EG relative to ethaline. The slower process for EG, τ_1, is again associated with the rotational decorrrelation of the EG molecule. Because it has a much shorter axis than Ch, the time scales are faster. Rotational motion of EG is much slower in ethaline than in the less viscous pure EG. Further analysis of these motions, including spectroscopic studies, may shed additional light on the dynamical processes of ethaline.

Table 2: Coefficients (time in ns) fitted to Eq. 8 for the dipole moment rotational dynamics based on CMD simulations at 298 K.

	b_1	α_1	b_2	α_2	τ_1	τ_2	R^2
				ethaline			
Ch	0.4716	0.9843	0.5284	0.7003	0.3534	0.0211	0.9989
EG	0.4436	0.9190	0.5564	0.7161	0.0801	0.0009	0.9953
				pure EG			
EG	0.5308	0.9807	0.4692	0.7606	0.0199	0.0004	0.9990

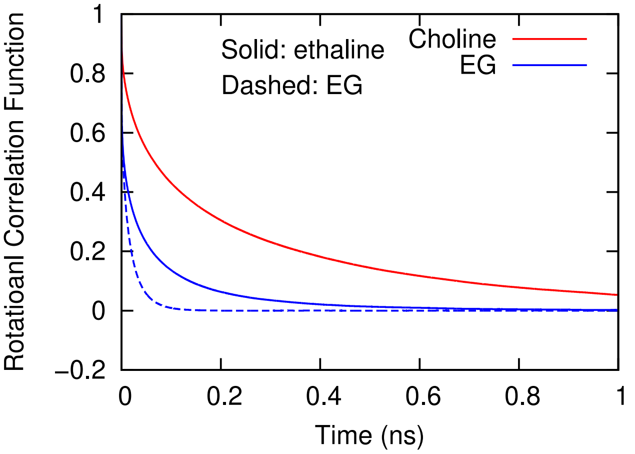

Figure 12: Normalized dipole moment rotational correlation function for choline and EG in ethaline (solid) and EG (dashed) calculated at 298 K.

Conclusions

A comprehensive study of the structure and dynamics of the 1:2 eutectic mixture of choline chloride and ethylene glycol (ethaline) has been carried out. Experimentally measured densities and viscosities match previously reported values very well. Classical and *ab initio* molecular dynamics simulations both capture experimental liquid structure, as determined by neutron scattering measurements. Computed diffusivities and viscosities also agree well with experiments. The simulations suggest that the solvation environment in ethaline is more complicated than what maybe assumed based on its stoichiometric composition. Addition of ChCl into pure EG breaks the HB network in EG and multiple types of HBs are formed. In particular, the HBs between Cl and EG hydroxyl groups were found to be stronger than those hydroxyl HBs in pure EG, resulting in higher viscosity and slower dynamics in ethaline compared to pure EG. The complex HBs in ethaline also cause complexity in dynamics. Rotational relaxation of choline is much slower than ethylene glycol. Dynamic heterogeneities persist for over 10 ns in ethaline, with the chloride ion experiencing the most dynamical heterogeneity due to its hydrogen bonding interactions.

Acknowledgement

This work was funded by Breakthrough Electrolytes for Energy Storage (BEES) - an Energy Frontier Research Center funded by the U.S. Department of Energy, Office of Science, Basic Energy Science under award number DE-SC0019409. A portion of this research used resources at the Spallation Neutron Source, a DOE Office of Science User Facility operated by the Oak Ridge National Laboratory. YZ, DP and EM thank the Center for Research Computing (CRC) at the University of Notre Dame for providing computational resources. BWD and MET thank the HPC center at New York University for providing computing resources.

References

(1) Nkuku, C. A.; LeSuer, R. J. Electrochemistry in Deep Eutectic Solvents. *J. Phys. Chem. B* **2007**, *111*, 13271–13277.

(2) Carriazo, D.; Serrano, M. C.; Gutierrez, M. C.; Ferrer, M. L.; del Monte, F. Deep-eutectic solvents playing multiple roles in the synthesis of polymers and related materials. *Chem. Soc. Rev.* **2012**, *41*, 4996–5014.

(3) Li, C.; Li, D.; Zou, S.; Li, Z.; Yin, J.; Wang, A.; Cui, Y.; Yao, Z.; Zhao, Q. Extraction desulfurization process of fuels with ammonium-based deep eutectic solvents. *Green Chem.* **2013**, *15*, 2793–2799.

(4) Singh, B.; Lobo, H.; Shankarling, G. Selective N-Alkylation of Aromatic Primary Amines Catalyzed by Bio-catalyst or Deep Eutectic Solvent. *Cat. Lett.* **2011**, *141*, 178–182.

(5) Smith, E. L.; Abbott, A. P.; Ryder, K. S. Deep Eutectic Solvents (DESs) and Their Applications. *Chem. Rev.* **2014**, *114*, 11060–11082.

(6) Leron, R. B.; Li, M. High-pressure volumetric properties of choline chloride-ethylene glycol based deep eutectic solvent and its mixtures with water. *Thermochim. Acta* **2012**, *546*, 54–60.

(7) Leron, R. B.; Soriano, A. N.; Li, M. Densities and refractive indices of the deep eutectic solvents (choline chloride + ethylene glycol or glycerol) and their aqueous mixtures at the temperature ranging from 298.15 to 333.15 K. *J. Taiwan. Inst. Chem. Eng.* **2012**, *43*, 551–557.

(8) Leron, R. B.; Li, M.-H. Molar heat capacities of choline chloride-based deep eutectic solvents and their binary mixtures with water. *Thermochim. Acta* **2012**, *530*, 52–57.

(9) Yadav, A.; Kar, J. R.; Verma, M.; Naqvi, S.; Pandey, S. Densities of aqueous mixtures of (choline chloride + ethylene glycol) and (choline chloride + malonic acid) deep eutectic solvents in temperature range 283.15-363.15K. *Thermochim. Acta* **2015**, *600*, 95–101.

(10) Mjalli, F. S.; Ahmed, O. U. Physical properties and intermolecular interaction of eutectic solvents binary mixtures: reline and ethaline. *Asia-Pac J. Chem. Eng.* **2016**, *11*, 549–557.

(11) Harifi-Mood, A. R.; Buchner, R. Density, viscosity, and conductivity of choline chloride plus ethylene glycol as a deep eutectic solvent and its binary mixtures with dimethyl sulfoxide. *J. Mol. Liq.* **2017**, *225*, 689–695.

(12) Lapena, D.; Lomba, L.; Artal, M.; Lafuente, C.; Giner, B. Thermophysical characterization of the deep eutectic solvent choline chloride:ethylene glycol and one of its mixtures with water. *Fluid Phase Equilibr.* **2019**, *492*, 1–9.

(13) Zahn, S.; Kirchner, B.; Mollenhauer, D. Charge Spreading in Deep Eutectic Solvents. *ChemPhysChem* **2016**, *17*, 3354–3358.

(14) Stefanovic, R.; Ludwig, M.; Webber, G. B.; Atkin, R.; Page, A. J. Nanostructure, hydrogen bonding and rheology in choline chloride deep eutectic solvents as a function of the hydrogen bond donor. *Phys. Chem. Chem. Phys.* **2017**, *19*, 3297–3306.

(15) Perkins, S. L.; Painter, P.; Colina, C. M. Experimental and computational studies of choline chloride-based deep eutectic solvents. *J. Chem. Eng. Data* **2014**, *59*, 3652–3662.

(16) Ferreira, E. S. C.; Voroshylova, I. V.; Pereira, C. M.; D. S. Cordeiro, M. N. Improved Force Field Model for the Deep Eutectic Solvent Ethaline: Reliable Physicochemical Properties. *J. Phys. Chem. B* **2016**, *120*, 10124–10137.

(17) Doherty, B.; Acevedo, O. OPLS Force Field for Choline Chloride-Based Deep Eutectic Solvents. *J. Phys. Chem. B* **2018**, *122*, 9982–9993.

(18) Kaur, S.; Malik, A.; Kashyap, H. K. Anatomy of Microscopic Structure of Ethaline Deep Eutectic Solvent Decoded through Molecular Dynamics Simulations. *J. Phys. Chem. B* **2019**, *123*, 8291–8299.

(19) Structural, Thermodynamic, and Transport Properties of Aqueous Reline and Ethaline Solutions from Molecular Dynamics Simulations. *Journal of Physical Chemistry B* **2019**, *123*, 11014–11025.

(20) Reuter, D.; Binder, C.; Lunkenheimer, P.; Loidl, A. Ionic conductivity of deep eutectic solvents: The role of orientational dynamics and glassy freezing. *Physical Chemistry Chemical Physics* **2019**, *21*.

(21) Faraone, A.; Wagle, D. V.; Baker, G. A.; Novak, E. C.; Ohl, M.; Reuter, D.; Lunkenheimer, P.; Loidl, A.; Mamontov, E. Glycerol Hydrogen-Bonding Network Dominates Structure and Collective Dynamics in a Deep Eutectic Solvent. *Journal of Physical Chemistry B* **2018**,

(22) Mukherjee, K.; Das, A.; Choudhury, S.; Barman, A.; Biswas, R. Dielectric Relaxations of (Acetamide + Electrolyte) Deep Eutectic Solvents in the Frequency Window, 0.2 v/GHz 50: Anion and Cation Dependence. *Journal of Physical Chemistry B* **2015**, *119*, 8063–8071.

(23) Mukherjee, K.; Das, S.; Tarif, E.; Barman, A.; Biswas, R. Dielectric relaxation in acetamide + urea deep eutectics and neat molten urea: Origin of time scales via temperature dependent measurements and computer simulations. *Journal of Chemical Physics* **2018**, *149*.

(24) Hossain, S. S.; Samanta, A. Solute Rotation and Translation Dynamics in an Ionic Deep Eutectic Solvent Based on Choline Chloride. *J. Phys. Chem. B* **2017**, *121*, 10556–10565.

(25) Hammond, O. S.; Bowron, D. T.; Edler, K. Liquid structure of the choline chloride-urea deep eutetic solvent (reline) from neutron diffraction and atomistic modelling. *Green Chem.* **2016**, *18*, 2736–2744.

(26) Lloyd, D.; Vainikka, T.; Kontturi, K. The development of an all copper hybrid redox flow battery using deep eutectic solvents. *Electrochim. Acta* **2013**, *100*, 18–23.

(27) Mirza, N. R.; Nicholas, N. J.; Wu, Y.; Mumford, K. A.; Kentish, S. E.; Stevens, G. W. Experiments and thermodynamic modeling of the solubility of carbon dioxide in three different deep eutectic solvents (DESs). *J. Chem. Eng. Data* **2015**, *60*, 3246–3252.

(28) Gao, M.; Yang, C.; Zhang, Q.; Yu, Y.; Hua, Y.; Li, Y.; Dong, P. Electrochemical fabrication of porous Ni-Cu alloy nanosheets with high catalytic activity for hydrogen evolution. *Electrochim. Acta* **2016**, *215*, 609–616.

(29) Gurkan, B.; Squire, H.; Pentzer, E. Metal-Free Deep Eutectic Solvents: Preparation, Physical Properties, and Significance. *Phys. Chem. Lett.* **2019**, *10*, 7956–7964.

(30) Tuckerman, M. E.; Yarne, D.; Samuelson, S. O.; Hughes, A. L.; Martyna, G. J. Exploiting multiple levels of parallelism in Molecular Dynamics based calculations via modern techniques and software paradigms on distributed memory computers. *Comput. Phys. Commun.* **2000**, *128*, 333–376.

(31) Martinez, J. M.; Martinez, L. Packing Optimization for Automated Generation of Complex System's Initial Configurations for Molecular Dynamics and Docking. *J. Comput. Chem.* **2003**, *24*, 819–825.

(32) Martinez, L.; Andrade, R.; Martinez, J. M. Software News and Update Packmol: A Package for Building Initial Configurations for Molecular Dynamics Simulations. *J. Comput. Chem.* **2009**, *30*, 2157–2164.

(33) Shahbaz, K.; Baroutian, S.; Mjalli, F.; Hashim, M.; AlNashef, I. Densities of ammonium and phosphonium based deep eutectic solvents: Prediction using artificial intelligence and group contribution techniques. *Thermochim. Acta* **2012**, *527*, 59–66.

(34) VandeVondele, J.; Krack, M.; Mohamed, F.; Parrinello, M.; Chassaing, T.; Hutter, J. Quickstep: Fast and accurate density functional calculations using a mixed Gaussian and plane waves approach. *Comput. Phys. Commun.* **2005**, *167*, 103–128.

(35) VandeVondele, J.; Hutter, J. Gaussian basis sets for accurate calculations on molecular systems in gas and condensed phases. *J. Chem. Phys.* **2007**, *127*, 114105.

(36) Perdew, J. P.; Burke, K.; Ernzerhof, M. Generalized Gradient Approximation Made Simple. *Phys. Rev. Lett.* **1996**, *77*, 3865–3868.

(37) Grimme, S.; Ehrlich, S.; Goerigk, L. Effect of the damping function in dispersion corrected density functional theory. *J. Comput. Chem.* **2011**, *32*, 1456–1465.

(38) Martyna, G. J.; Klein, M. L.; Tuckerman, M. Nosé–Hoover chains: The canonical ensemble via continuous dynamics. *J. Chem. Phys.* **1992**, *97*, 2635–2643.

(39) Nosé, S. A unified formulation of the constant temperature molecular dynamics methods. *J. Chem. Phys.* **1984**, *81*, 511–519.

(40) Brehm, M.; Kirchner, B. TRAVIS - A Free Analyzer and Visualizer for Monte Carlo and Molecular Dynamics Trajectories. *J. Chem. Inf. Model.* **2011**, *51*, 2007–2023.

(41) Plimpton, S. Fast Parallel Algorithms for Short-range Molecular Dynamics. *J. Comput. Phys.* **1995**, *117*, 1–19.

(42) Wang, J.; Wolf, R. M.; Caldwell, J. W.; Kollman, P. A.; Case, D. A. Development and Testing of a General Amber Force Field. *J. Comput. Chem.* **2004**, *25*, 1157–1174.

(43) Zhang, Y.; Maginn, E. J. A Simple AIMD Approach to Derive Atomic Charges for Condensed Phase Simulation of Ionic Liquids. *J. Phys. Chem. B* **2012**, *116*, 10036–10048.

(44) Hockney, R.; Eastwood, J. *Computer simulation using particles*; Adam Hilger, New York, 1989.

(45) Sun, H. COMPASS: An ab Initio Force-Field Optimized for Condensed-Phase ApplicationssOverview with Details on Alkane and Benzene Compounds. *J. Phys. Chem. B* **1998**, *102*, 7338–7364.

(46) Hoover, W. G. Canonical Dynamics: Equilibrium Phase-space Distributions. *Phys. Rev. A* **1985**, *31*, 1695–1697.

(47) Shinoda, W.; Shiga, M.; Mikami, M. Rapid Estimation of Elastic Constants by Molecular Dynamics Simulation under Constant Stress. *Phys. Rev. B* **2004**, *69*, 134103.

(48) Zhang, Y.; Zhang, Y.; McCready, M. J.; Maginn, E. J. Evaluation and refinement of the general AMBER Force Field for nineteen pure organic electrolyte solvents. *J. Chem. Eng. Data* **2018**, *63*, 3488–3502.

(49) Szefczyk, B.; Cordeiro, M. N. D. Physical properties at the base for the development of an all-atom force field for ethylene glycol. *J. Phys. Chem. B* **2011**, *115*, 3013–3019.

(50) Shahbaz, K.; Baroutian, S.; Mjalli, F.; Hashim, M.; AlNashef, I. Densities of ammonium and phosphonium based deep eutectic solvents: prediction using artificial intelligence and group contribution techniques. *Thermochim. Acta* **2012**, *527*, 59–66.

(51) Shahbaz, K.; Mjalli, F.; Hashim, M.; AlNashef, I. Prediction of deep euteric solvents densities at different temperatures. *Thermochim. Acta* **2011**, *515*, 67–72.

(52) Mjalli, F.; Vakili-Nezhaad, G.; Shahbaz, K.; AlNashef, I. Application of the Eotvos and Guggenheim empirical rules for predicting the density and surface tension of ionic liquids analogues. *Thermochim. Acta* **2014**, *575*, 40–44.

(53) Sears, V. F. Neutron scattering lengths and cross sections. *Neutron News* **1992**, *3*, 26–37.

(54) Lorch, E. Neutron Diffraction by Germania Silica and Radiation-Damaged Silica Glasses. *J. Phys. C: Solid State Phys.* **1969**, *2*, 229–237.

(55) Korotkevich, A.; Firaha, D. S.; Padua, A. A.; Kirchner, B. Ab initio molecular dynamics simulations of SO2 solvation in choline chloride/glycerol deep eutectic solvent. *Fluid Phase Equilibr.* **2017**, *448*, 59–68.

(56) Lide, D. R., Ed. *CRC handbook of chemistry and physics, Internet Version 2005, http://www.hbcpnetbase.com*; CRC Press, Boca Raton, FL, 2005.

(57) Mjalli, F. S.; Naser, J. Viscosity model for choline chloride-based deep eutectic solvents. *Asia-Pac. J. Chem. Eng.* **2015**, *10*, 273–281.

(58) Zhang, Y.; Otani, A.; Maginn, E. J. Reliable Viscosity Calculation from Equilibrium Molecular Dynamics Simulations: A Time Decomposition Method. *J. Chem. Theory Comput.* **2015**, *11*, 3537–3546.

(59) Rey-Castro, C.; Vega, L. F. Transport Properties of Ionic Liquid 1-ethyl-3-methylimidazolium Chloride from Equilibrium Molecular Dynamics Simulation. The Effect of Temperature. *J. Phys. Chem. B* **2006**, *110*, 14426–14435.

(60) Del Popolo, M.; Voth, G. On the Structure and Dynamics of Ionic Liquids. *J. Phys. Chem. B* **2004**, *108*, 1744–1752.

(61) Jiang, W.; Yan, T.; Wang, Y.; Voth, G. A. Molecular dynamics simulation of the energetic room-temperature ionic liquid, 1-hydroxyethyl-4-amino-1,2,4-triazolium nitrate (HEATN). *J. Phys. Chem. B* **2008**, *112*, 3121–3131.

(62) Shukla, A.; Prajapati, J. On a generalization of Mittag-Leffler function and its properties. *J. Math. Anal. Appl.* **2007**, *336*, 797–811.

(63) Gorenflo, R.; Loutchko, J.; Luchko, Y. Computation of the Mittag-Leffler function E,(z) and its derivative. *FRACT. CALC. APPL. ANAL* 2002.

(64) Hilfer, R.; Anton, L. Fractional master equations and fractal-time random walks. *Phys. Rev. E* **1995**, *51*, R848.

(65) Metzler, R.; Klafter, J. The random walk's guide to anomalous diffusion: a fractional dynamics approach. *Phys. Rep.* **2000**, *339*, 1–77.

(66) Hilfer, F. Fractional diffusion based on Riemann-Liouville fractional derivatives. *J. Phys. Chem. B* **2000**, *104*, 3914–3917.

(67) Tuckerman, M. E.; Chandra, A.; Marx, D. A statistical mechanical theory of proton transport kinetics in hydrogen-bonded networks based on population correlation functions with applications to acids and bases. *J. Chem. Phys.* **2010**, *133*, 124108.

(68) Hopfenmuller, B.; Zorn, R.; Holderer, O.; Ivanova, O.; Lehnert, W.; Luke, W.; Ehlers, G.; Jalavro, N.; Schneider, G. J.; Monkenbusch, M.; Richter, D. Fractal diffusion in high temperature polymer electrolyte fuel cell membranes. *J. Chem. Phys.* **2018**, *148*, 204906.